Supporting Information

Topological Insulator-Based van der Waals Heterostructures for Effective Control of Massless and Massive Dirac Fermions

*Su Kong Chong[1], Kyu Bum Han[2], Akira Nagaoka[2,3], Ryuichi Tsuchikawa[1], Renlong Liu[4,5], Haoliang Liu[1], Zeev Valy Vardeny[1], Dmytro A. Pesin[1], Changgu Lee[4,5], Taylor D. Sparks[2] and Vikram V. Deshpande[1]**

[1]Department of Physics and Astronomy, University of Utah, Salt Lake City, Utah 84112 USA

[2]Department of Materials Science and Engineering, University of Utah, Salt Lake City, Utah 84112 USA

[3]Department of Materials Science and Engineering, Kyoto University, Kyoto 606-8501, Japan

[4]Department of Mechanical Engineering, Sungkyunkwan University, 2066, Seobu-ro, Jangan-gu, Suwon, Gyeonggi, 16419, Republic of Korea

[5]SKKU Advanced Institute of Nanotechnology, Sungkyunkwan University, 2066, Seobu-ro, Jangan-gu, Suwon, Gyeonggi, 16419, Republic of Korea

*Corresponding author: E-mail: vdesh@physics.utah.edu; Phone number: 801-581-6570

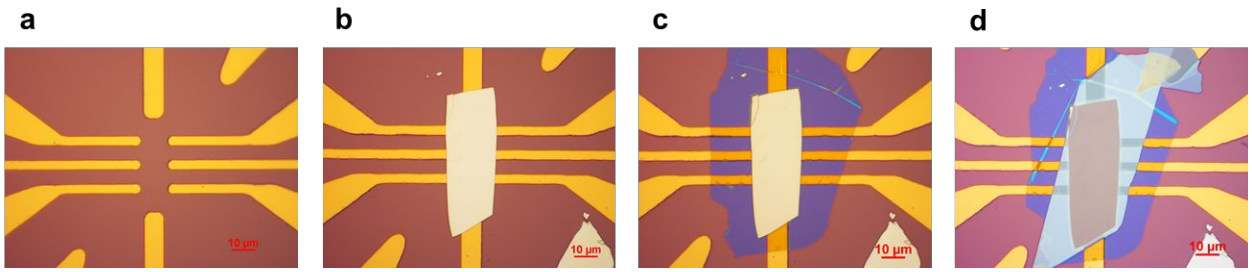

Figure S1 Device fabrication process. (a) The gold contact electrodes in Hall bar geometry were fabricated using a standard electron beam lithography on a SiO_2 (300 nm) coated Si substrate. (b) A BSTS flake exfoliated from the single crystal BSTS was transferred onto the pre-patterned electrodes using a home-built micro-manipulation stage. (c) A hBN flake exfoliated from a single crystal hBN was then transferred on the BSTS. (d) A graphite flake was transferred on the hBN at about 95^{o}C with the heating on the Si substrate, and joined to a gate electrode.

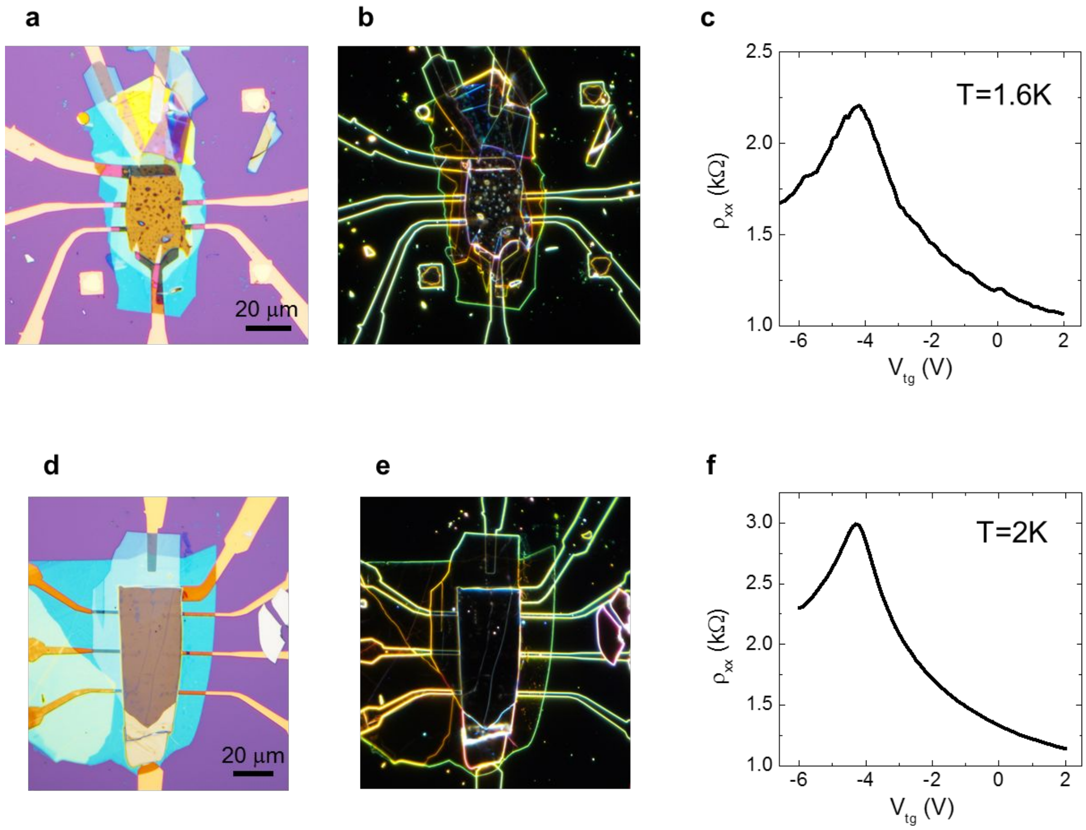

Figure S2 Effect of heterostructure interfaces on the transport properties. The representative (a, d) bright-field, and (b, e) dark-field optical images of a BSTS/hBN/graphite heterostructure with the graphite layer transferred at (room temperature, 95^{o}C heating). The blisters formation at the hBN-graphite interface is prevented by the high temperature (close to the vaporization of water) transfer. The (c, f) four-probe resistivities (ρ_{xx}) as a function of gate-voltage applied through the graphite gate-electrode for the BSTS (with, without) blisters forming at the hBN-graphite interface. With the same thickness of hBN (28 nm) layer, the sharper ρ_{xx} peak in (f) is attributed to the cleaner interface of the vdW heterostructure layers, resulting in a higher gating efficiency through the hBN/graphite gate.

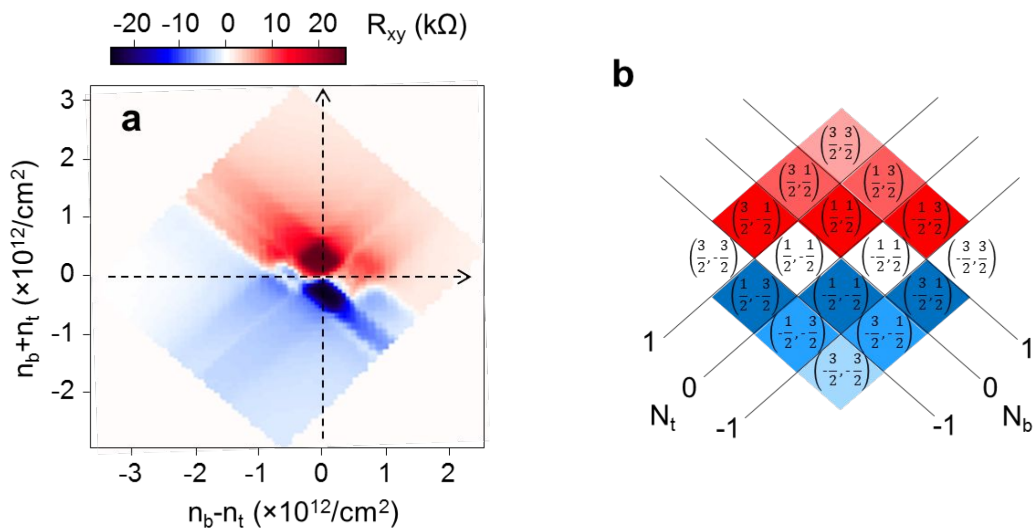

Figure S3 Quantization of Hall resistance from top and bottom surface states. (a) 2D color map of the Hall resistance (R_{xy}) as a function of sum and difference of the charge densities of the top (n_t) and bottom (n_b) surfaces. The vertical and horizontal dashed line arrows cross the symmetric and antisymmetric Landau Level filling factors between top (ν_t) and bottom (ν_b) surface states. (b) The quantization in R_{xy} is illustrated by a Landau level filling color schematic for the top and bottom surface states. The (ν_t, ν_b) of the corresponding Landau level indices of the top (N_t) and bottom (N_b) surface states are labeled in (b).

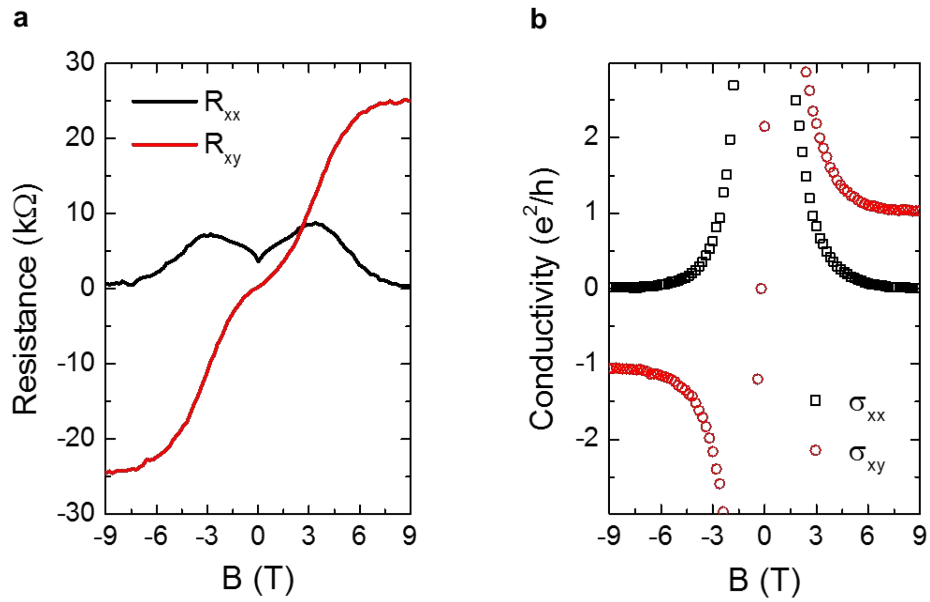

Figure S4 Magnetic field dependent QHE. (a) R_{xx} & R_{xy}, and (b) σ_{xx} & σ_{xy} as a function of magnetic field for the BSTS/hBN/graphite device. The R_{xx} (σ_{xx}) and R_{xy} (σ_{xy}) are highly-symmetrical and antisymmetrical, respectively, in opposite magnetic field. The σ_{xy} approaches quantum limit of e^2/h ($-e^2/h$), together with the vanishing in σ_{xx}, at magnetic field greater than 6T (-6T).

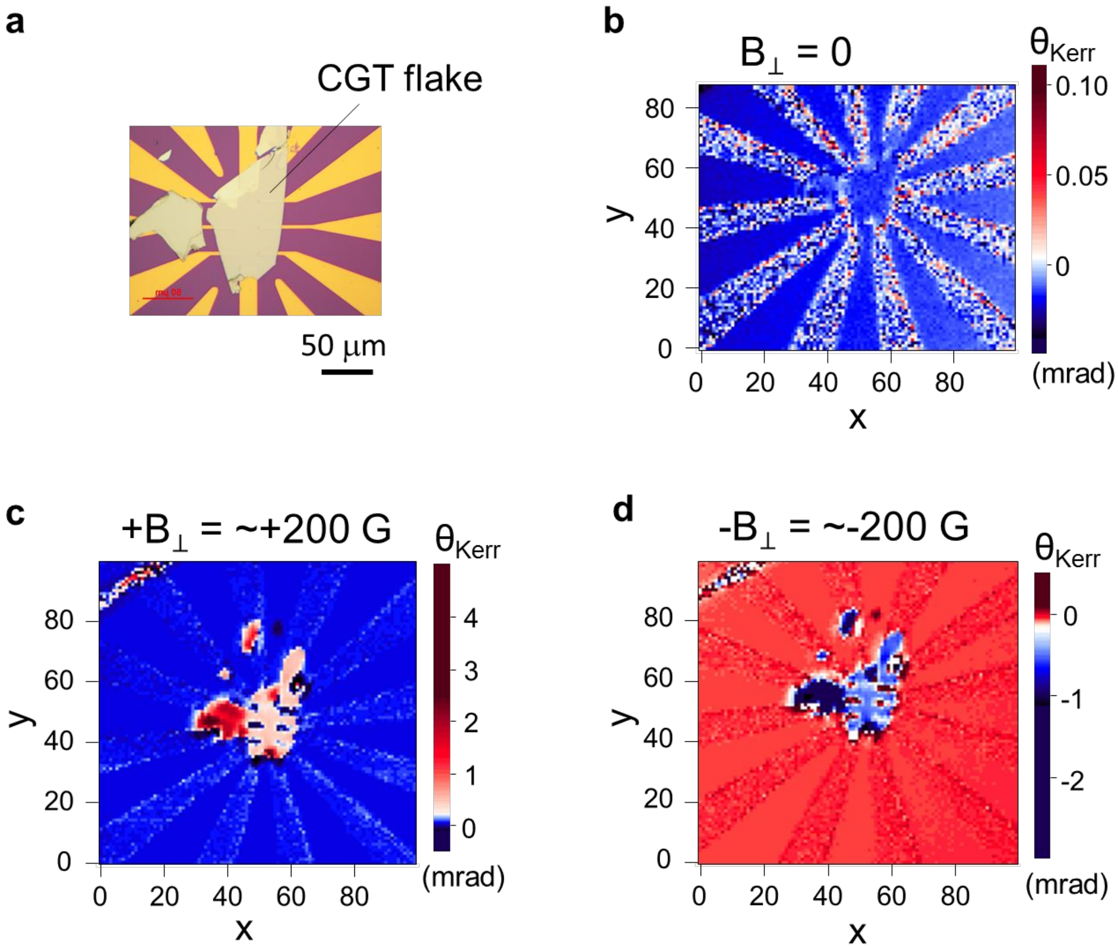

Figure S5 Kerr rotation studies of a $Cr_2Ge_2Te_6$ (CGT) flake. The magnetic properties of a 80 nm thick CGT flake (a) were studied using a Sagnac interferometer at cryogenic temperature. 2D spatial mapping of Kerr rotation angles (θ_{Kerr}) for the CGT device measured at (b) 0 G, (c) ~+200 G and (d) ~-200 G out of plane magnetic field. The large θ_{Kerr} detected and the antisymmetrical of θ_{Kerr} in opposite magnetic field confirm its ferromagnetic behavior.

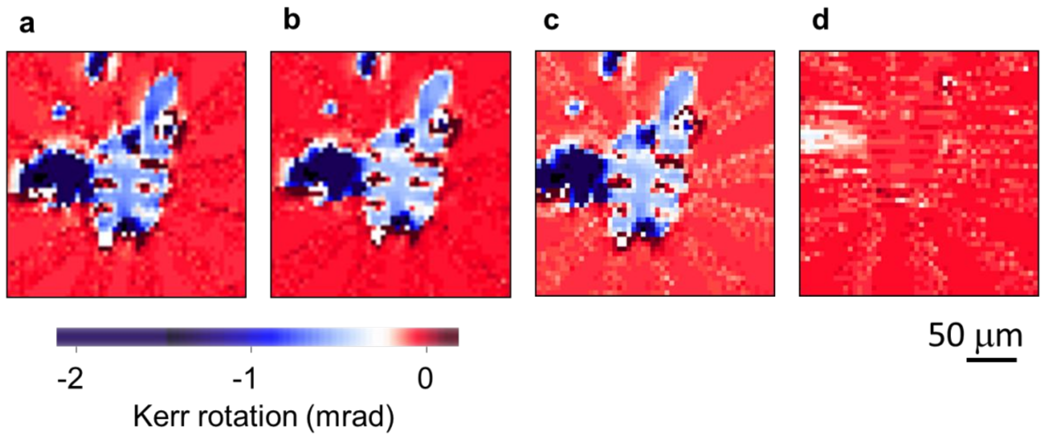

Figure S6 Temperature dependent Kerr rotation of a CGT flake. 2D maps of Kerr rotation angle (θ_{Kerr}) of the 80 nm CGT device measured at different temperature of (a) 4.7 K, (b) 20 K, (c) 60 K and (d) 80 K. The vanishing of θ_{Kerr} at 80 K indicates that the ferromagnetic phase transition occurred at a temperature between 60 to 80 K.

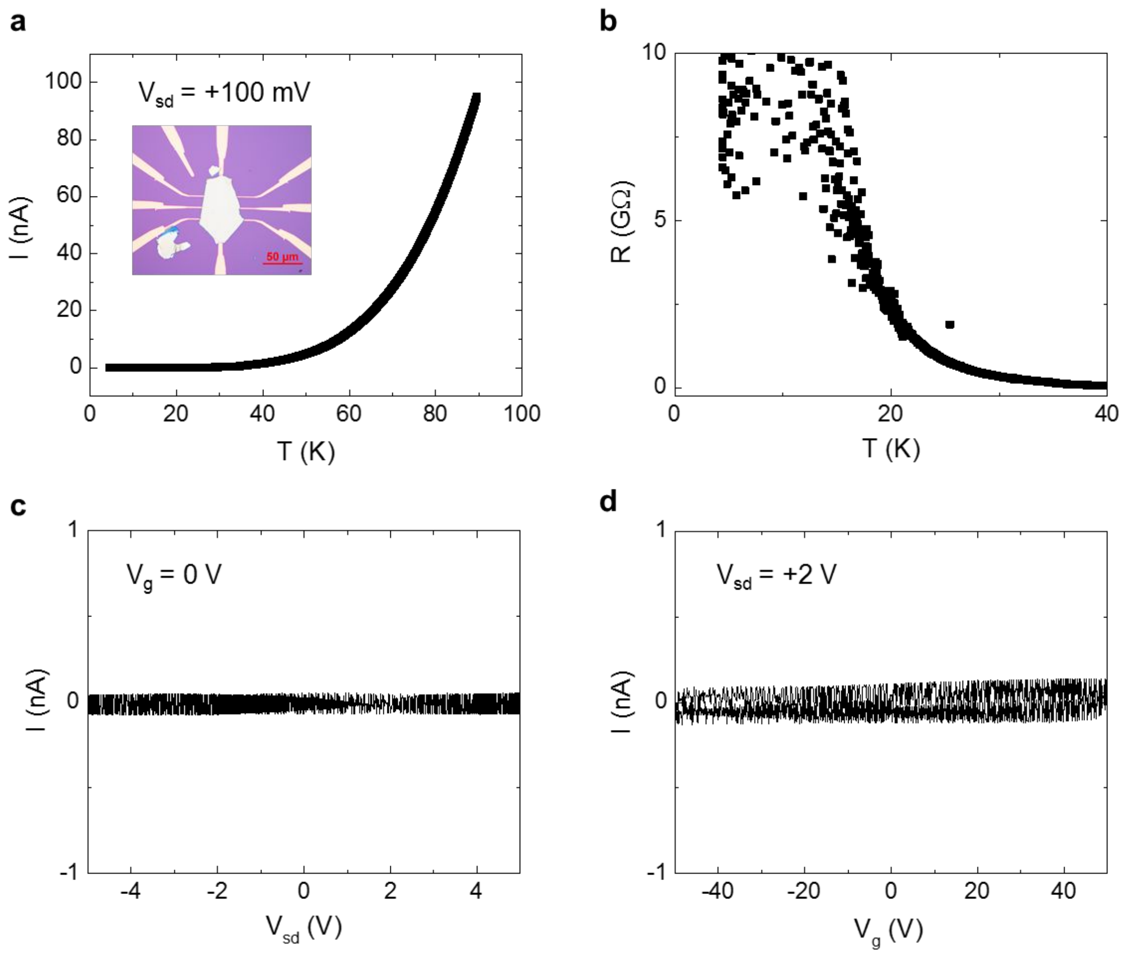

Figure S7 Transport properties of a single crystal $Cr_2Ge_2Te_6$ (CGT) flake. (a) Source-drain current (I) of a 120 nm CGT device (shown in the inset) as a function of temperature, measured at a fixed source-drain voltage of +100 mV. (b) The resistance (R) of the CGT device as a function of temperature shows the insulating behavior with R excceding 2 GΩ at temperature below 20 K. (c) The source-drain I versus V of the CGT device measured at temperature of 4 K. No source-drain I detected in the range of V_{sd} applied (±5V), showing the truly insulating of the CGT at cryogenic temperature. (d) The source-drain I as a function of gate voltage (V_g) applied through the Si/SiO_2 gate. No source-drain I detected indicates that the CGT is in the electronic band gap region within the range of V_g applied.

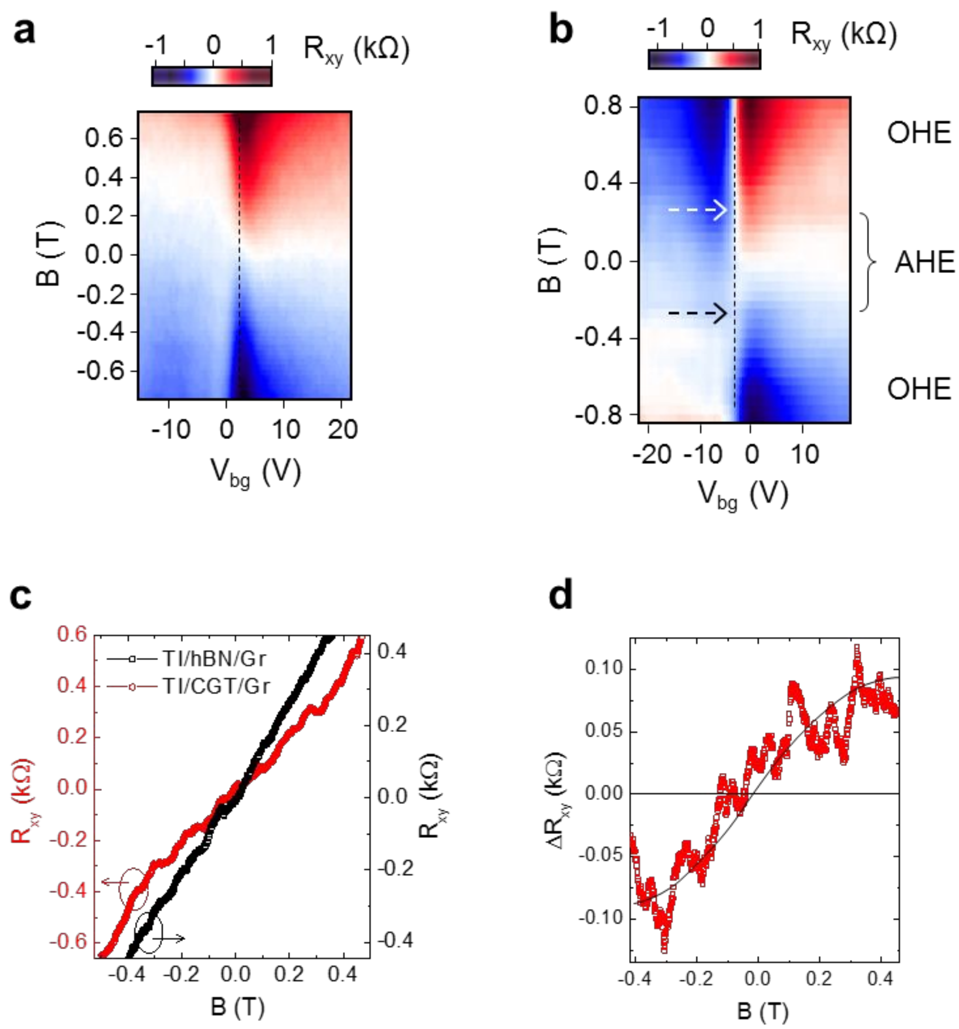

Figure S8 Anomalous Hall effect of a BSTS/CGT/Gr device. Color maps of the Hall resistance (R_{xy}) of the (a) BSTS/hBN/Gr, and (b) BSTS/CGT/Gr devices as a function of magnetic field and backgate voltage. The ordinary Hall effect (OHE) and anomalous Hall effect (AHE) regions were labeled in the figure. (c) Comparison of the R_{xy} at low magnetic field (±0.5 T) for the BSTS/hBN/Gr and BSTS/CGT/Gr devices. The different slope of R_{xy} vs B in BSTS/CGT/Gr device plot at low magnetic field range of about ±0.3 T is a result of the AHE. (d) The difference between R_{xy} of BSTS/hBN/Gr and BSTS/CGT/Gr (ΔR_{xy}) as a function of magnetic field. The black curve is a guide to the eyes to show the antisymetrical of ΔR_{xy} in the opposite magnetic field.

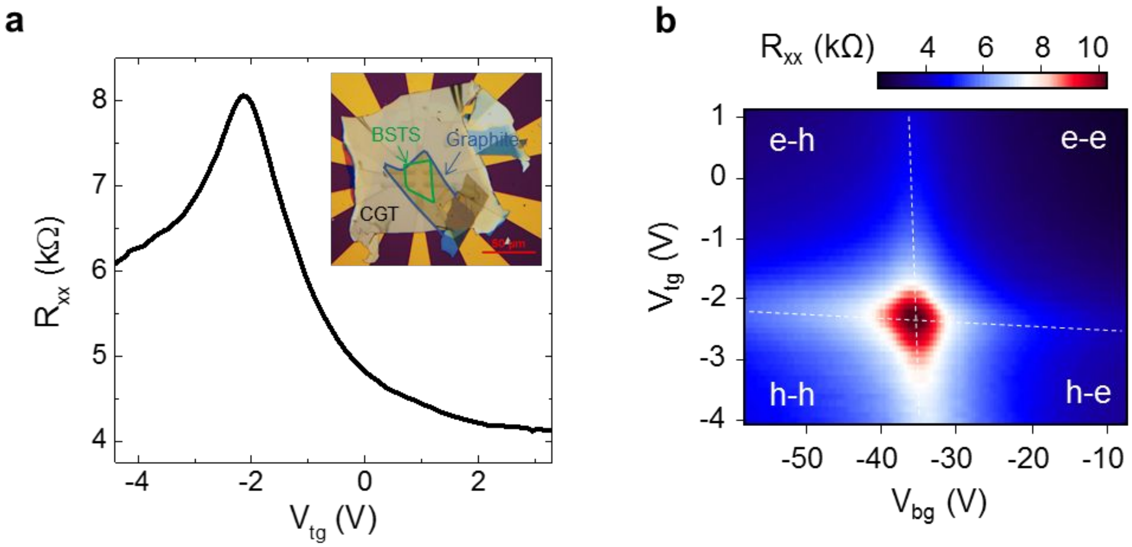

Figure S9 Gate-dependent resistance of a BSTS/CGT/Gr device. (a) Four-probe resistance (R_{xx}) of the BSTS as a function of V_{tg} applied through a CGT dielectric (thickness ~250 nm) measured at temperature of 1.6 K. Inset in (a) is the optical images of the device. (b) Color plot of the R_{xx} of the BSTS as a function of dual-gate voltages with the topgate as CGT/graphite and backgate as SiO_2/Si. Similar to the BSTS/hBN/Gr device, the top and bottom surface states can be tuned into the four quadrant conductions as labeled in (b).

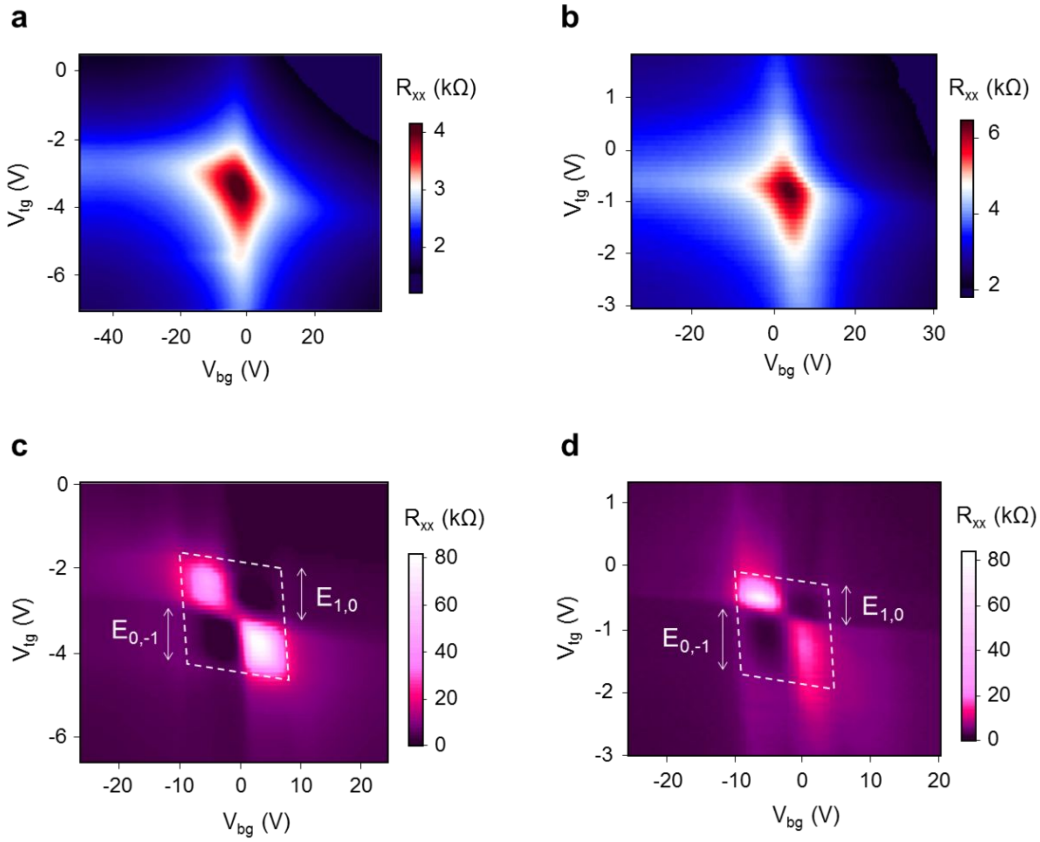

Figure S10 Estimation of the magnetic gap from dual-gated transport. Dual-gated color maps of longitudinal resistance (R_{xx}) for (a, c) BSTS/hBN/Gr_2, and (b, d) BSTS/CGT/Gr_2 devices measured at magnetic field of 0 and 9T. The thickness of the hBN and CGT layers are about 20 nm and 200 nm, respectively. Different from the hBN/Gr gating, the top surface tuned by CGT/Gr shows an irregular LL spacing between N_t=-1 to 0 and N_t=0 to +1. The magnetic exchange gap induced by the 2D ferromagnet CGT is evaluated from the difference between the $E_{0,-1}$ and $E_{1,0}$ LL spacing. The $E_{1,0}$ is calculated from the LL energy, $E_1 - E_0 = \sqrt{2e\hbar v_F^2 B} \approx$ 34.8 meV, where the Fermi velocity (v_F) is ~3.2×10^5 m/s. The $E_{0,-1}$ is expressed as $E_{0,-1} = E_{-1} - E_0 + \Delta$, where $E_{-1} = E_1$ and Δ is the magnetic exchange gap. The Δ is estimated to be about 18 meV.

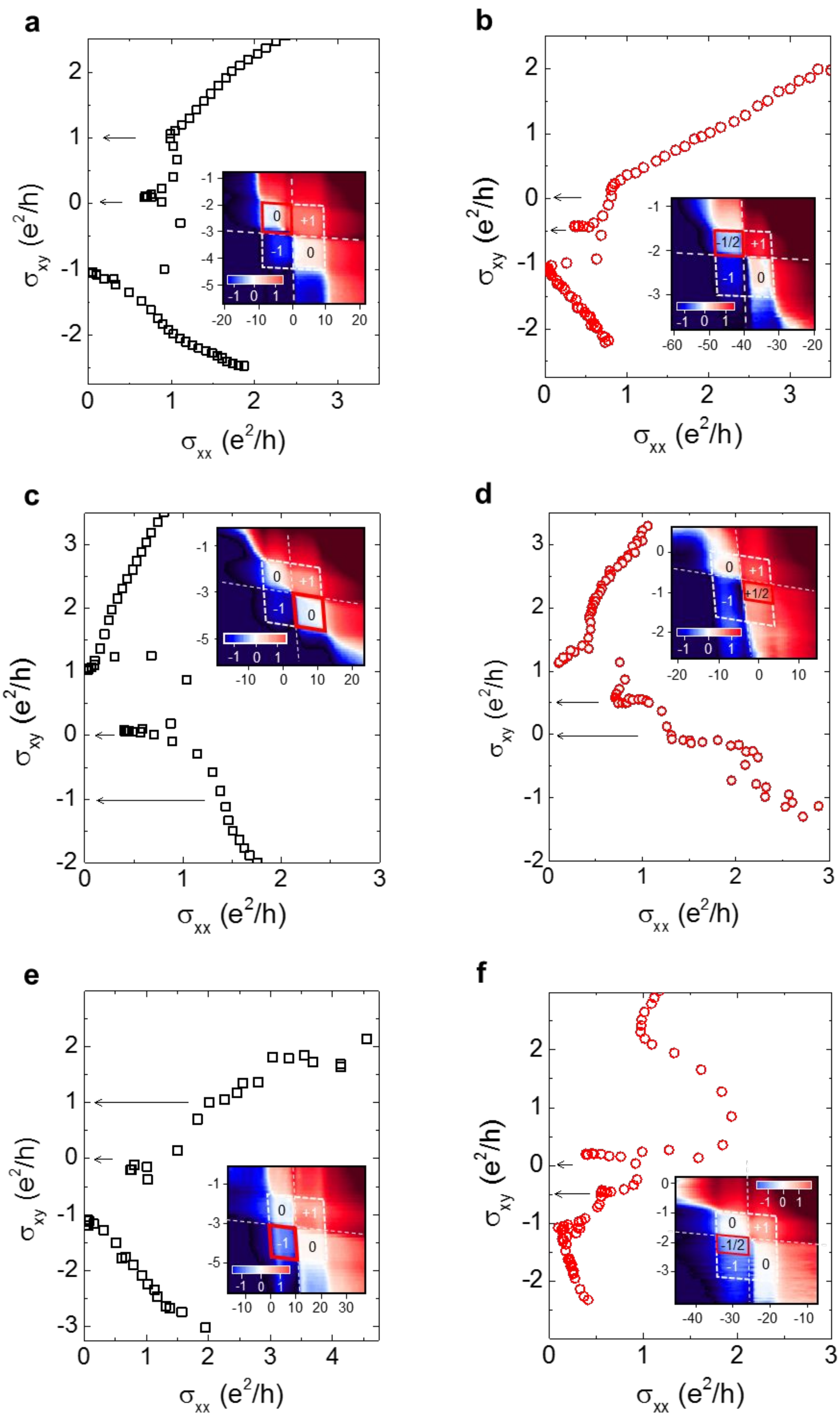
a
b
c
d
e
f
σxy (e²/h)
σxx (e²/h)
0
+1
-1
-1/2
+1/2

Figure S11 Renormalization group flow plots for various BSTS devices. The σ_{xy} versus σ_{xx} plots for three BSTS/hBN/Gr devices (a) BSTS/hBN/Gr_1, (c) BSTS/hBN/Gr_2, and (e) BSTS/hBN/Gr_3, and three BSTS/CGT/Gr devices (b) BSTS/CGT/Gr_1, (d) BSTS/CGT/Gr_2, and (f) BSTS/CGT/Gr_3, measured at 9T. Thickness of hBN and CGT are in the range of 18-23 nm and 200-300 nm, respectively. The dual-gated σ_{xy} color maps of the respective devices are inserted in the figures. The BSTS/hBN/Gr devices all show regular spaced integer quantum Hall plateaus developed near the center Dirac point. In comparison, the BSTS/CGT/Gr devices display the irregular quantum Hall plateaus with the extended ν= -1 compared to ν= +1 plateaus. The half-integer quantization plateau are consistently observed near or in the magnetic gap region in all the CGT-coupled BSTS devices. The renormalization group flow plots in (b), (d) and (f) all show half-integer -½ (or +½) features developed between ν= -1 (or +1) and 0.

Table S1. Device specifications of the BSTS/hBN/Gr and BSTS/CGT/Gr devices. The thicknesses of the BSTS ($\mathbf{d_{BSTS}}$), top gate dielectric layers of hBN ($\mathbf{d_{hBN}}$) or CGT ($\mathbf{d_{CGT}}$) flakes are measured using a Bruker Dimension Icon atomic force microscopy.

Device label	$\mathbf{d_{BSTS}}$ (nm)	$\mathbf{d_{hBN}}$ (nm)	$\mathbf{d_{CGT}}$ (nm)
BSTS/hBN/Gr_1	100	18	-
BSTS/hBN/Gr_2	61	16	-
BSTS/hBN/Gr_3	105	22	-
BSTS/hBN/Gr_4	80	18	-
BSTS/hBN/Gr_5	120	17	-
BSTS/hBN/Gr_6	135	20	-
BSTS/CGT/Gr_1	112	-	160
BSTS/CGT/Gr_2	68	-	130
BSTS/CGT/Gr_3	120	-	200